Corrosion Science 119 (2017) 1–13

Contents lists available at ScienceDirect

Corrosion Science

journal homepage: www.elsevier.com/locate/corsci

In-situ electrochemical impedance spectroscopy measurements of zirconium alloy oxide conductivity: Relationship to hydrogen pickup

Adrien Couet [a,*], Arthur T. Motta [b], Antoine Ambard [c], Didier Livigni [c]

[a] Department of Engineering Physics, University of Wisconsin-Madison, Madison, WI 53715, USA
[b] Department of Mechanical and Nuclear Engineering, Penn State University, University Park, PA 16802, USA
[c] EDF Research and Development, Materials and Mechanics of Components, Ecuelles, 77818 Moret-sur-Loing, France

ARTICLE INFO

Article history:
Received 22 September 2016
Received in revised form
18 December 2016
Accepted 20 December 2016
Available online 23 December 2016

Keywords:
Hydrogen pickup
Fuel cladding corrosion
EIS
Oxide resistivity

ABSTRACT

Hydrogen pickup during nuclear fuel cladding corrosion is a critical life-limiting degradation mechanism for nuclear fuel. Following a program dedicated to zirconium alloys, corrosion, it has been hypothesized that oxide electronic resistivity determines hydrogen pickup. In-situ electrochemical impedance spectroscopy experiments were performed on Zircaloy-4 and Zr-2.5Nb alloys in 360 °C water. The oxide resistivity was measured as function of time. The results show that as the oxide resistivity increases so does the hydrogen pickup fraction. The resistivity of the oxide layer formed on Zircaloy-4 is higher than on Zr-2.5Nb, resulting in a higher hydrogen pickup fraction of Zircaloy-4, compared to Zr-2.5Nb.

Published by Elsevier Ltd.

1. Introduction and motivation

1.1. Introduction

Hydrogen pick-up during nuclear fuel cladding corrosion is a critical life-limiting degradation mechanism for nuclear fuel in existing and advanced nuclear reactors. Indeed, hydrogen ingress can cause cladding embrittlement by brittle hydride precipitation in the zirconium metal, and limit cladding lifetime [1]. Although it is understood that different alloys exhibit not only different corrosion kinetics, but also different hydrogen pickup rates at different stages of corrosion [2–5], a complete understanding of the role of alloying elements in the corrosion and hydrogen pick-up mechanisms is still lacking. It is also known that the corrosion performance of zirconium alloys worsens as the alloy purity increases and almost any alloying addition (even in very small proportions) increases corrosion resistance [6]. On the other hand, these additions can have dramatic effects on hydrogen pickup, with Nb additions usually resulting in significant reductions in hydrogen pickup [7]. This study investigates the mechanistic links between hydrogen pick-up and alloying elements using in-situ electrochemistry impedance spectroscopy (EIS) on two oxide layers formed during autoclave corrosion of two different zirconium alloys: Zircaloy-4 and Zr-2.5Nb.

1.2. Review of zirconium oxide resistivity measurements in Zr alloys by EIS

Although many EIS studies have been performed on zirconium oxide scales, because of obvious experimental difficulties few of these have been conducted at operating conditions and for long exposure times [8–12]. A brief review of the main conclusions from previous studies is presented in the following.

The measurements performed at high temperatures on thermally grown oxides which have been conducted to date show that EIS is a suitable technique to follow the oxidation kinetics in situ. Indeed, by extrapolating the capacitance at infinite frequency or from a Cole–Cole diagram, it is generally possible to monitor the oxidation kinetics in-situ [13]. However, it has been shown that quantitative oxide thickness estimations are rather difficult to obtain by these methods. Thus, in general, an arbitrary capacitance is chosen, which, after fitting, matches the known oxide thickness for that particular alloy. These impedance results are generally in very good agreement with the oxide thickness determined by Scanning Electron Microscopy (SEM) and/or weight gain [10,12]. All studies also concluded that the oxide capacitance shows a significant dispersion such that the oxide dielectric permittivity appears to depend on frequency [13]. Because of the resulting difficulty

* Corresponding author.
E-mail address: couet@wisc.edu (A. Couet).

http://dx.doi.org/10.1016/j.corsci.2016.12.008
0010-938X/Published by Elsevier Ltd.

Table 1
Composition of Zircaloy-4 and Zr-2.5Nb tube alloys.

Alloy	Nominal Alloy Composition (weight percent)			
	Sn	Nb	Fe	Cr
Zircaloy-4	1.45		0.2	0.1
Zr-2.5Nb		2.5		

in correctly fitting the impedance spectra, the oxide capacitance is usually modeled by the constant phase elements (CPE) method rather than a pure capacitance model, even though the physical meaning of CPE is still a matter of debate [14].

The detailed analysis of EIS spectra support the theory of a bi-layered oxide with different oxide layer properties: a very thin (a few nm) protective inner layer and an outer porous non-protective layer. This model has been proposed as the only one to successfully reproduce the impedance measurements [8,12]. However, no general agreement on the oxidation kinetics has been reached in the literature, which puts into question the nature of this model. Also, this postulated very thin (~10 nm) inner protective layer does not correlate with electron microscopy observations of zirconium alloy oxides [15,16].

Finally, it has generally been observed that oxide impedance measured at low frequency increases with exposure time. By assuming that the low frequency impedance is related to the inverse of the oxidation rate [12], it is concluded that the resistance to charged species transport across the oxide layer increases with the oxide thickness [10]. This is expected, since the flux of charged species across the oxide decreases as the oxide thickness increases [17].

The electronic resistivity of yttria stabilized ZrO_2 at 400 °C has been calculated as being approximately equal to 10^5 Ω cm [18]. To explain their EIS results, Gohr et al. [8] have hypothesized that the quality (related to conductivity – inverse of resistivity in Ω cm) of the oxide layer degrades as the oxide thickens in the protective regimes. However, the modeling of the electrochemical circuit using EIS measurements is rather difficult and no consensus has been reached as to how the electrochemical response can be interpreted in terms of oxide layer properties [10]. It is thus critical to demonstrate the capability of evaluating oxide layer properties of interest from EIS measurements before drawing any conclusions.

1.3. Alloys studied

Zircaloy-4 and Zr-2.5Nb tube alloys are studied in this paper (see alloy compositions in Table 1). The manufacturing process and microstructure characterizations were specified in detail in [2] for these two alloys. They are both precipitate forming alloys ($Zr(Fe,Cr)_2$ precipitates in Zircaloy-4 and βNb precipitates in Zr-2.5Nb) and are fully recrystallized, with a grain size diameter approximately equal to 10 μm.

1.4. Corrosion experiment and measurements

To compare the hydrogen pickup of different alloys, it is necessary to quantify the amount of hydrogen picked up relative to the amount of corrosion. Thus, the oxidation rate (measured from weight gain) and hydrogen uptake (precisely measured from vacuum hot extraction and cold neutron prompt gamma activation experiments) were determined as a function of exposure time for a set of zirconium alloys corroded in a static autoclave (360 °C, 18 MPa, pure water, H_2 ~ 30 cc/kgH_2O) [2,19]. 4 bar of hydrogen were inserted in the overhead gas of the static autoclave at the start of the experiment, which corresponds to approximately 30 cc/kgH_2O at equilibrium at high temperatures [20]. The total hydrogen pickup fraction f_H^t, defined as the ratio of the hydrogen absorbed from the beginning of the corrosion test to the total amount of hydrogen generated by the corrosion, was calculated for the two alloys. The oxidation kinetics and total hydrogen pickup fraction are plotted in Fig. 1 for the two alloys as function of exposure time. The power law fits are also shown and it is clearly observed that Zircaloy-4 oxidation kinetics are cubic (or even sub-cubic) while Zr-2.5Nb are higher than cubic (n = 0.37) and thus closer to parabolic as already observed previously [2,3].

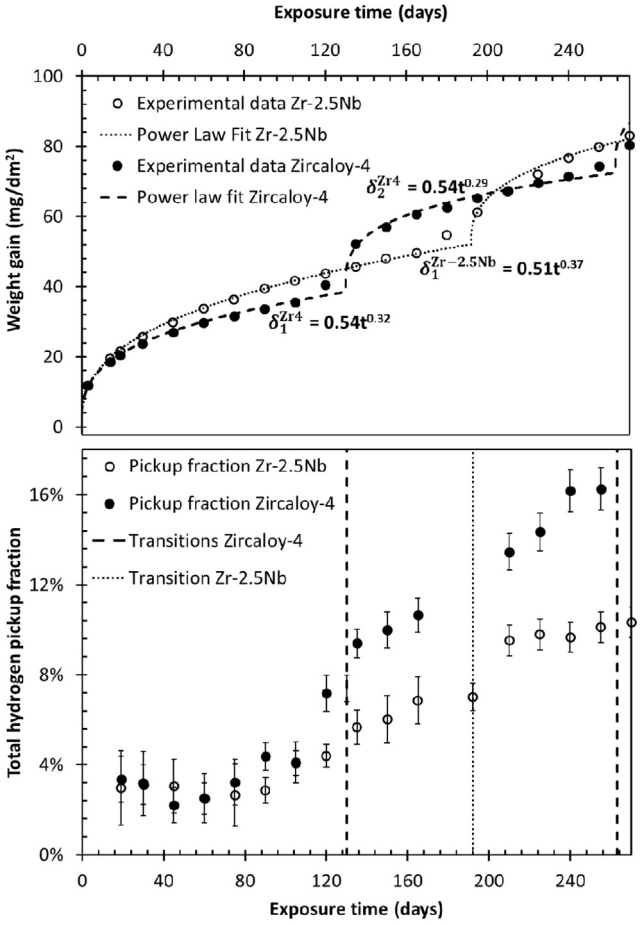

Fig. 1. Weight gain (and power law fits $\delta = kt^n$) and total hydrogen pickup fractions measurements of Zircaloy-4 and Zr-2.5Nb alloys as function of exposure time. The oxidation rate transitions are also indicated on the total hydrogen pickup fraction plot.

It is useful to plot the results in a manner that allows easy comparison of f_H^t between Zircaloy-4 and Zr-2.5Nb as the two alloys develop oxide layers of similar thicknesses, but following different kinetics. Fig. 2 shows the hydrogen content plotted as function of the weight gain (or oxide thickness). Note that the dotted lines correspond to different levels of constant f_H^t. From Figs. 1 and 2 it is clear that the f_H^t of Zr4 is consistently higher than that of ZrNb, indicating that alloying elements have a significant impact on hydrogen pickup mechanism. It has also been previously shown that the total hydrogen pick-up fraction increases during corrosion [21].

Comparison between alloys has also shown that the alloying elements present in the alloy are closely related to the oxidation kinetics of the alloy (as measured, for example, by the value of the corrosion exponent n of the power law fit) and to the hydrogen pick-up fraction [21]. Because the oxidation state of the alloying elements in the oxide varies with distance from the oxide-metal interface it is logical to expect that overall oxide resistivity varies as a function of oxide depth and exposure time (possibly as a result of oxide doping) [22]. However, the understanding of the specific

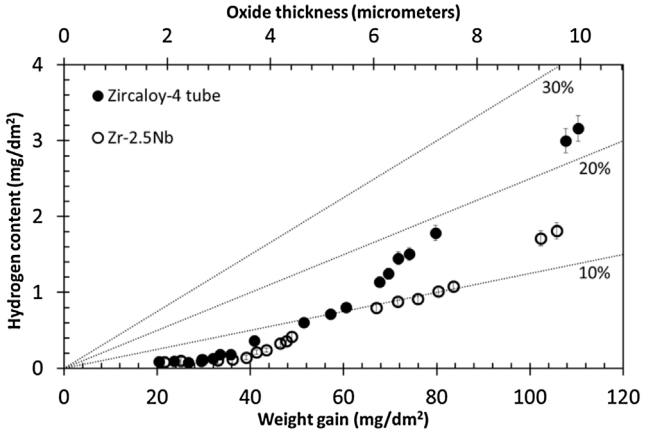

Fig. 2. Hydrogen content of Zircaloy-4 and Zr-2.5Nb as function of oxide thickness. Dotted lines represent constant hydrogen pickup fraction.

effect of oxide doping on the zirconium oxide electronic resistivity is still lacking [23–26].

2. General hypothesis

As a result of these observations, it has been hypothesized that oxide electronic resistivity and alloying elements (either in second phase particles – SPP – or in solid solution) determine the corrosion kinetics and hydrogen pickup. The oxide electronic resistivity would create the driver for hydrogen uptake (the driving force being the electric potential across the oxide). The alloying elements present in solid solution in the oxide and possibly in SPP incorporated in the oxide layer can impact the oxide resistivity [17,27]. Basically, the location of the cathodic reaction (whether close to the oxide/metal interface (for high oxide electronic resistivity) or close to the oxide/water interface (for low oxide electronic resistivity)) has a significant impact on the hydrogen uptake by the metal. According to this hypothesis hydrogen pickup increases when electron transport becomes more difficult, requiring hydrogen ingress to close the cathodic reaction. Thus, the electronic resistivity of the protective oxide is a key parameter to control the oxidation kinetics and hydrogen pickup [8,21,28]. The potential gradient acts to increase (resp. reduce) the flux of the oxygen vacancies (resp. electrons) through the protective oxide layer. As shown schematically in Fig. 3, a low (resp. high) oxide electronic resistivity results in a low (resp. high) oxide electric potential, which in return increases (resp. decreases) the interfacial potential at the oxide/water interface. Indeed, the corrosion potential (given by $V_{W/O} - V_{M/O}$) is fixed, as the system boundaries are supposed to be at thermodynamic equilibrium (an assumption to be verified later). However, the repartition of the potential in the system can vary between the interfacial drops and the potential in the oxide as indicated by the dotted curves in Fig. 3.[1] That is why a higher oxide resistivity will reduce the interfacial drop at the oxide/water interface, reducing the activation energy for hydrogen absorption. In summary, a high (resp. low) oxide electronic resistivity will increase (resp. reduce) the driving force for hydrogen absorption.

In the present study, the variation of the oxide electronic resistivity as a function of exposure time for Zircaloy-4 and Zr-2.5Nb alloys was measured using in-situ Electrochemical Impedance Spectroscopy (EIS). These impedance measurements are compared

[1] In Fig. 3, the electric field is supposed to be constant across the oxide (i.e. slope of the potential curve is constant) but this is correct only if one assumes space charges effects on corrosion kinetics are not significant. This validity of that assumption depends on the alloys considered as detailed in [17,27,29].

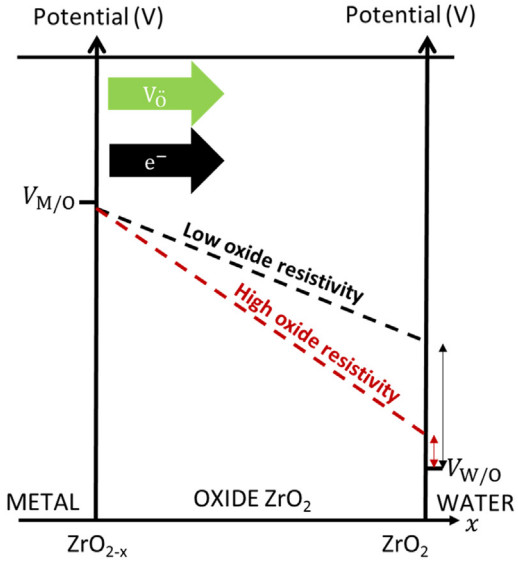

Fig. 3. Scheme of the hydrogen pickup driving force for low and high oxide electronic resistivity.

with the evolution of hydrogen pickup fraction as function of exposure time to assess the possible correlation between oxide resistivity and hydrogen pickup fraction.

It should be noted that this scenario is based on the very general assumption that corrosion and hydriding of zirconium result from the movement of charged species. Neutral species are disregarded in the following.

3. EIS experimental setup

Fig. 4 presents a schematic diagram of the EIS experimental setup. Electrical feedthroughs were provided by Pt wires in cooled Teflon seal elements at the top of the autoclave. Zirconium alloy tubes served as the working electrodes. A perforated Pt cylinder served as coaxial *quasi*-reference electrode. This Pt electrode was

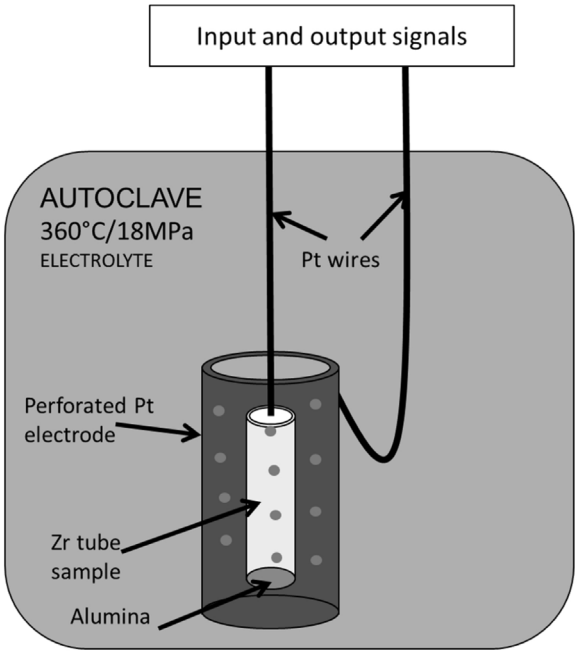

Fig. 4. Schematic diagram of the EIS experimental setup.

placed at an approximate distance of 0.5 mm between the electrodes leading to a symmetrical two-electrode configuration.

A two-electrode cell was used, since electrochemical reactions at the Pt electrode are much faster than at the Zr electrode making the Pt electrode a very good *quasi*-reference electrode. Tube ends were isolated with spring-loaded Al_2O_3 ceramic caps, leaving an exposed outer surface area of about 8 cm^2. The connectivity between the tubes and the Pt wire was maintained by welding a Zr-Sn wire to the inside of the tube. This configuration was adopted for both experiments in the Zircaloy-4 and the Zr-2.5Nb tubes. Information about processing, metallurgy and microstructure of these alloys can be found in [2]. As shown in Figs. 1 and 2, the oxide thicknesses and hydrogen pickup fractions of these alloys have been previously measured as function of exposure time in the exact same conditions [2,30]. A Pt/Pt dummy cell of identical geometry was used for electrolyte conductivity monitoring. The contribution of the Pt electrode to the total impedance of the Zr/Pt cell measured with the dummy cell consisting of two electrodes in series is negligible. EIS measurements were acquired at the open-circuit potential at frequencies of about 10^{-4}–10^{6} Hz in a floating configuration (U_{ac} = 50 mV) with a PAR4000® potentiostat.

4. Measurements of oxide properties from in-situ EIS spectra

All EIS spectra shown here have been acquired in-situ at 360 °C. Before extracting oxide properties from EIS spectra analysis (i.e. oxide resistivity ρ_{ox}), it is necessary to carefully validate that the oxide property of interest is indeed reflected in the EIS spectra. This is the subject of this entire section, which, although lengthy, is critical to validate the results presented. A more detailed analysis can be found in [31].

4.1. General assumptions on the system impedance Z_t

Assuming the oxide is a single dense and homogeneous phase, the system under study in this experiment can be well represented by pure circuit elements (resistance and capacitance) such that the overall impedance is approximated as:

$$Z_t = R_m + R_e + \sum_{\substack{ox/e,\\ i=\ ox,\\ ox/m}} \frac{R_i}{1+j\omega C_i R_i} \tag{1}$$

with Z_t the total system impedance, R_i and C_i the pure resistance and capacitance of metal (m), electrolyte (e), oxide (ox) and both oxide interface (ox/e and ox/m), $j^2 = -1$ and ω the signal pulsation (rad s^{-1}). The electrolyte – here nearly pure water – capacitance does not appear in the frequency range investigated in this study because:

$$1/C_e R_e \gg 10^6 \text{Hz} \rightarrow R_e/(1+j\omega C_e R_e) \sim R_e \tag{2}$$

From (1):

$$\lim_{\omega\to\infty} Z_t \sim R_m + R_e \text{ and } \lim_{\omega\to 0} Z_t \sim R_m + R_e + \sum_{\substack{ox/e,\\ i=\ ox,\\ ox/m}} R_i \tag{3}$$

The electrical conductivity of the weld contact between the wire and the tube was measured under dry conditions before corrosion and after 10 days in the autoclave. The impedance measurements show no signs of accelerated corrosion of the weld contact after exposure in the autoclave and its impedance over the entire frequency range of interest was negligible (~0.5 Ω) compared to the total impedance of the specimen. The metal resistivity can also be neglected: $R_m \sim 0$ and $\lim_{\omega\to\infty} Z_t \sim R_e$. Additional experimental validations that $\lim_{\omega\to\infty} Z_t \sim R_e$ are provided in the Appendix A.

The double layer at the oxide/electrolyte interface is only a few nanometers thick [32] and can be expressed via the plane capacitor formula:

$$C_{dl} = \frac{\varepsilon_{dl}\varepsilon_0 S}{\delta_{dl}} \tag{4}$$

where C_{dl} is the double layer capacitance at the oxide/electrolyte interface (in F), ε_{dl} the relative permittivity of the double layer, ε_0 the vacuum permittivity (in F m^{-1}), S the surface of the interface (in cm^2) and δ_{dl} the thickness of the double layer (in cm).

The oxide capacitance can be derived similarly:

$$C_{ox} = \frac{\varepsilon_{ox}\varepsilon_0 S}{\delta_{ox}} \tag{5}$$

where the terms are defined as in the double layer case in (4) but for the oxide. Given that the double layer is extremely thin compared to the oxide thickness, $\delta_{dl} \ll \delta_{ox}$, and since the relative permittivities ε_{ox} and ε_{dl} are of the same order of magnitude and the surface is the same in both systems, comparing (4) and (5), it is verified that $C_{dl} \gg C_{ox}$ .The double layer reciprocal capacitance at the interfaces can be neglected compared to the oxide reciprocal capacitance at relatively high frequency.

$$Z_t(\omega \gg 1) \sim R_e + \sum_{\substack{ox/e,\\ i=\ ox,\\ ox/m}} \frac{1}{j\omega C_i} = R_e - \frac{j}{\omega C_{ox}} \tag{6}$$

The Fermi level of zirconium metal is close to the conduction band of zirconium oxide resulting in a negligible Schottky barrier at the oxide/metal interface. Indeed, the charge transfer impedance at the interface is expected to be negligible at low frequency [25,33]. Thus the resistivity of the charge transfer at the oxide/metal interface is negligible at low frequency:

$$\lim_{\omega\to 0} Z_t \sim R_e + \sum_{\substack{ox/e,\\ i=\ ox}} R_i \tag{7}$$

4.2. EIS spectra processing

An example of Bode plots acquired on the Zr-2.5Nb alloy corroded for 62 days is shown in Fig. 5 . The open circled represent raw EIS data (represented as Bode plots) and are similar to those observed in previous experiments [10,12].

The filled symbols represent processed EIS data in which $\lim_{\omega\to\infty} Z_t \sim R_e$ has been subtracted from the whole spectra. As a summary, the total system impedance can be approximated depending on the frequency range as illustrated in Table 2.

In conclusion it appears theoretically possible to extract C_{ox} (i.e δ_{ox} using (5)) from the *imaginary part of the impedance at relatively high frequency* $\text{Im}(Z_t(\omega \gg 1))$ and a convolution of $R_{ox/e} + R_{ox}$ *from the real part of the impedance at zero frequency* $\text{Re}\left(\lim_{\omega\to 0} Z_t\right)$. This is the subject of the next section.

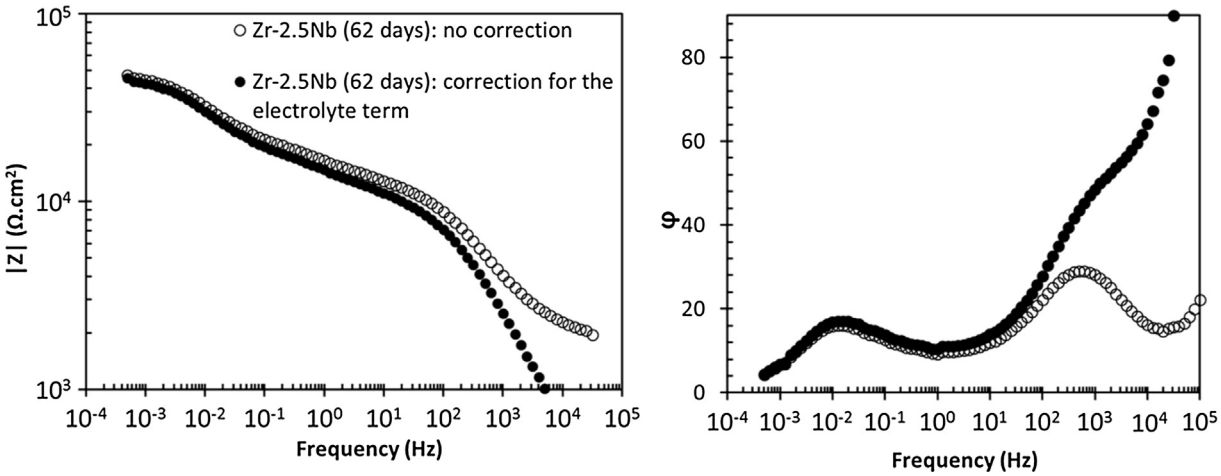

Fig. 5. Impedance modulus and phase as function of frequency of Zr-2.5Nb. The open circles are raw data, and the filled symbols are corrected for the electrolyte resistance R_e.

4.3. Validation of δ_{ox} and ρ_{ox} measurements from EIS spectra analysis

4.3.1. Zirconium alloys impedance spectra as function of exposure time

Impedance spectra have been acquired every week during a total of 325 days of exposure for Zr-2.5Nb alloy and 288 days of exposure for Zircaloy-4 alloy. The acquisition time of each spectrum is approximately one day, so that the system is considered to be at steady state during the acquisition. A selection of EIS spectra for both alloys is presented below.

4.3.1.1. Zircaloy-4. Fig. 6 shows the impedance modulus and the phase (corrected for the electrolyte resistance – see above) plotted at different exposure times, as calculated from raw EIS spectra for the Zircaloy-4 alloy. On each set of Bode plots, the weight gain data from Fig. 1 are also plotted with the exposure time range related to the specific Bode plots marked by a grey area in each one.

It is observed in Fig. 6 that the real impedance modulus at low frequency tends towards a plateau as the phase goes to zero, indicating a pure resistive behavior of the system. This trend was expected from the theory [34] as the low frequency impedance of the system is a combination of the interfacial oxide/water resistance and the bulk oxide resistance (see Table 2). Thus, in order to determine the bulk oxide resistance, one needs to evaluate the significance of the oxide/water interfacial resistance. It is observed in Fig. 6(a)–(e) that both the modulus and the phase of the electrochemical response evolve with exposure time and oxide thickness. From the analysis it is clear that the modulus of the oxide layer impedance in Fig. 6(a), (c) and (e) increases as the protective oxide thickness increases. However, analyzing Fig. 6(b) and (d), the oxide impedance modulus significantly decreases during the total period plotted of approximately 30 days. This decrease is clearly correlated to the two observed oxide transitions, which occur at those periods. The impedance modulus decrease is gradual and starts approximately at the same time as the increase in weight gain as observed in weight gain plots of Fig. 6(b) and (d). Thus, the evolution of the low frequency impedance (related to the oxide impedance through (7)) is clearly inversely proportional to the corrosion rate. This conclusion provides a first strong argument that R_{ox}, the resistance of the bulk oxide layer, has a significant contribution in $\lim_{\omega\to 0} Z_t$.

The impedance phase also evolves as function of oxide thickness. Two phase relaxation peaks are consistently observed, with largely different time dependences: one, remaining at 1 kHz and the other shifting from 100mHz to 1mHz as the protective oxide grows. This relaxation peak frequency is thus clearly dependent on oxide thickness. Considering the relaxation peak phase shifts, the 1 kHz peak phase shift increases (and the lower frequency peak phase shift decreases) as the protective oxide grows. This relaxation peak frequency thus depends on the oxide thickness. These trends are reversed during oxide transition. These two relaxation peaks have been previously observed at the exact same frequencies in [10].

4.3.1.2. Zr-2.5Nb. The impedance modulus for the Zr-2.5Nb alloy (corrected for the electrolyte resistance) and the phase for different exposure times are plotted in Fig. 7. Unfortunately, because of experimental difficulties, no impedance spectra were recorded before 72 days. The oxidation kinetics are also plotted, as was done in Fig. 6. The same impedance variations observed in Zircaloy-4, are observed in Zr-2.5Nb impedance spectra. In this case also, the oxide transition is marked by a gradual decrease of the impedance modulus whereas the growth of the protective oxide is marked by an increase in the impedance modulus especially at low frequency. Similarly to the Zircaloy-4 observation, this conclusion provides a strong argument that R_{ox} has a significant contribution in $\lim_{\omega\to 0} Z_t$. Considering the phase, the same relaxation peaks are observed, one remaining at 1 kHz, and the other shifting from 100mHz to 1mHz.

Table 2
Approximated total system impedance as function of the EIS frequency domain.

Frequency domain	$\omega \to 0$	$\omega \gg 1$	$\omega \to \infty$
Approximated total impedance	$R_e + \sum_{i=ox/e,ox} R_i$	$R_e - \frac{j}{\omega C_{ox}}$	R_e
Approximated impedance after processing $(Z_t - \lim_{\omega\to\infty} Z_t)$	$\sum_{i=ox/e,ox} R_i$	$-\frac{j}{\omega C_{ox}}$	0

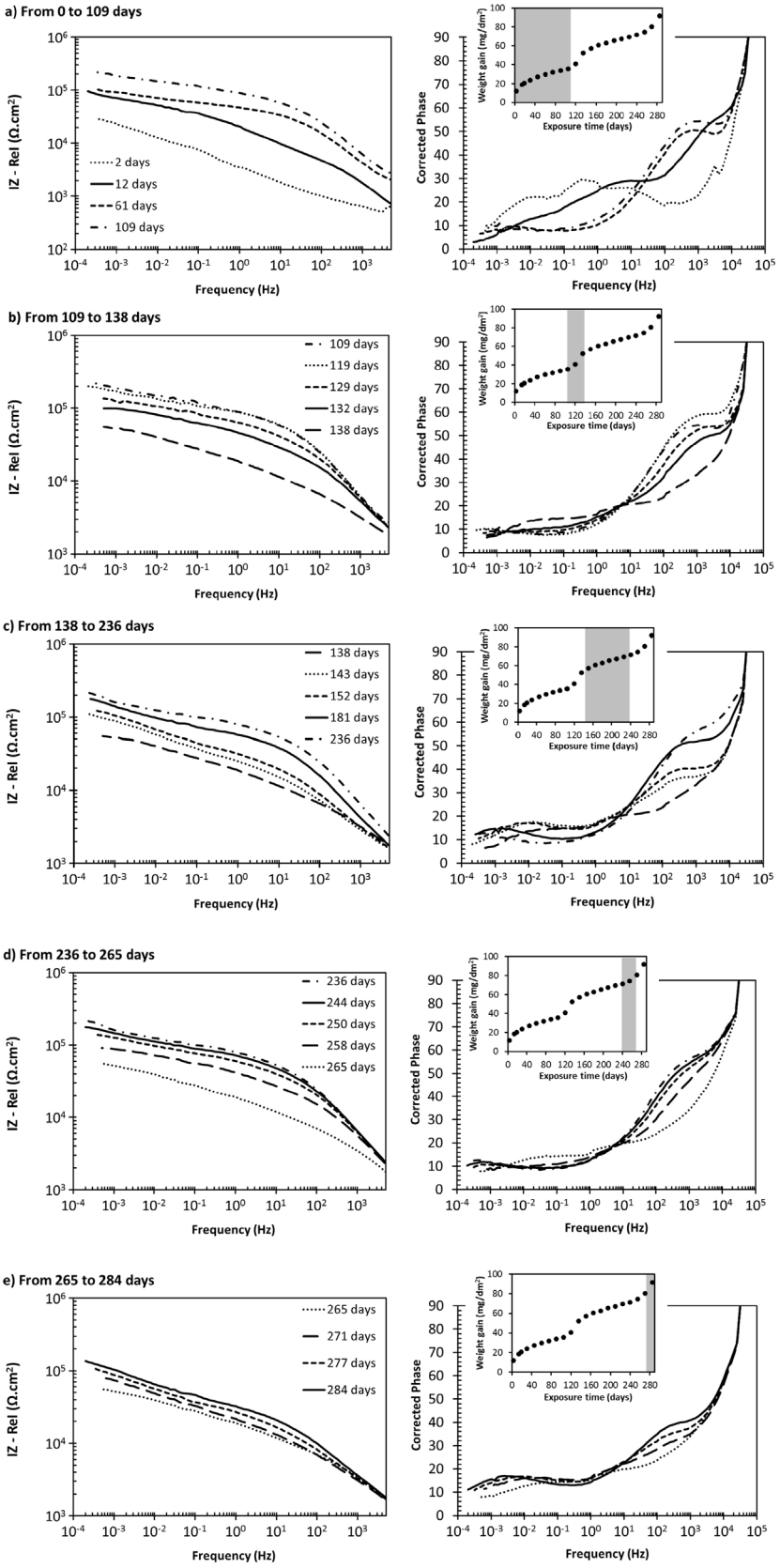

Fig. 6. Zircaloy-4 impedance modulus and phase (corrected for the electrolyte resistance) at different times: (a) from 0 to 109 days, (b) from 109 to 138 days, (c) from 138 to 236 days, (d) from 236 to 265 days, (e) from 265 to 284 days. The corresponding oxidation kinetics are marked by a grey area on the weight gain plots.

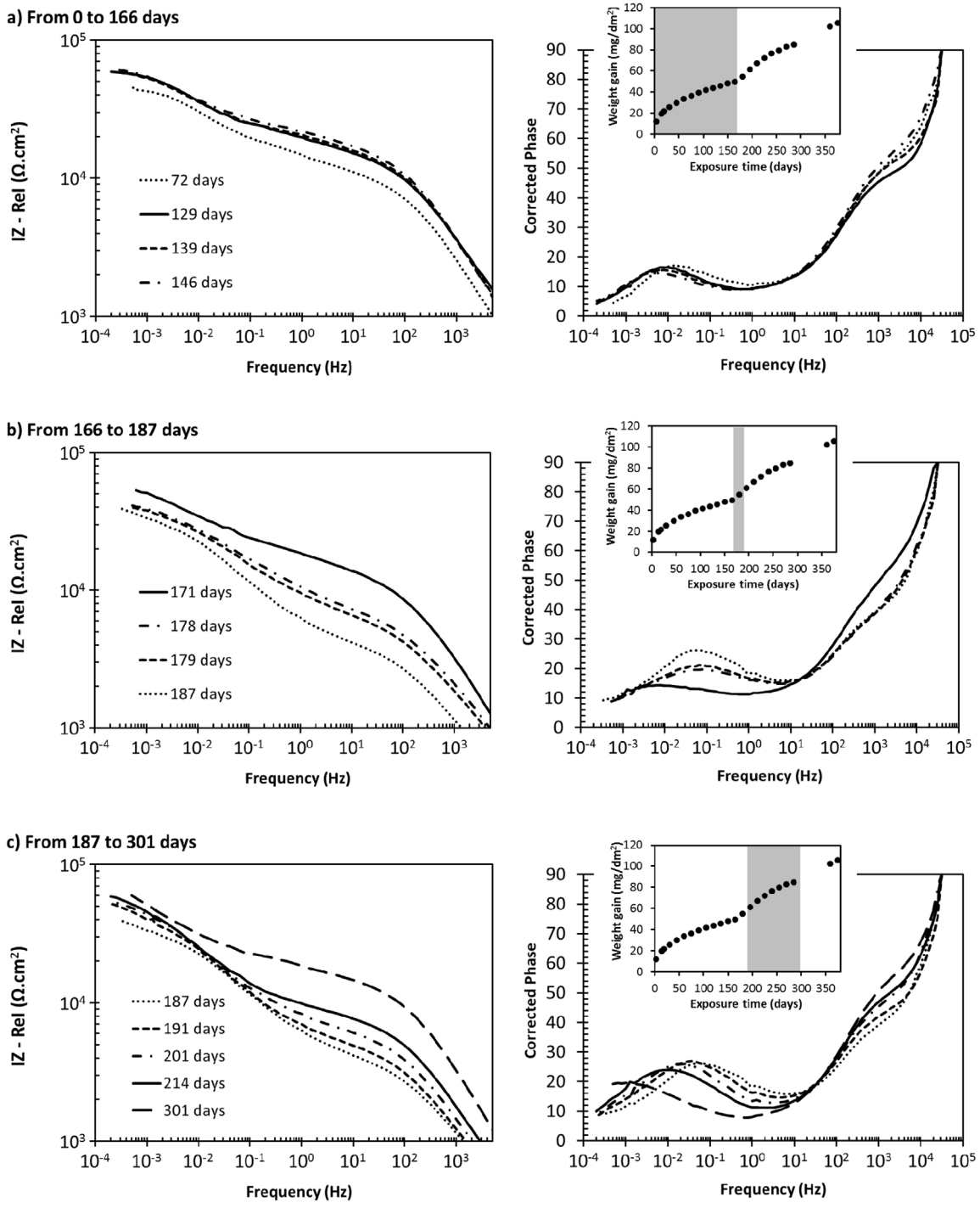

Fig. 7. Zr-2.5Nb modulus and phase (corrected for the electrolyte resistance) at different times: (a) from 0 to 166 days, (b) from 166 to 187 days, (c) from 187 to 301 days. The corresponding oxidation kinetics in each case are marked by a grey area on the weight gain plots.

According to Table 2, it should be possible to extract the oxide thickness in-situ at different exposure times by extracting $\mathrm{Im}(Z_t(\omega \gg 1))$ in Figs. 6 and 7 and applying (6) and (5). This is the subject of the next section.

4.3.2. Protective oxide thickness measurements

The oxide layer at high frequencies can be considered as a pure capacitor such that the real capacitance at high frequency can be ideally related to the oxide thickness by the plane capacitor Formula (5).

Since the oxide thickness can also be derived from weight gain measurements (see Fig. 1), it is possible to verify the validity of the EIS measurements and data processing. To evaluate the capacitance at high frequency, different methods are available, such as the Cole–Cole extrapolation [9]. It is also possible to obtain a trend of the variation of oxide thickness from the evaluation of the reciprocal series capacitance $1/C_{ox}$ (deduced from the imaginary impedance: $1/C_{ox} = j\omega \mathrm{Im}(Z_t)$ from (6)) at high frequency [10] where $\mathrm{Im}(Z_t)$ is the imaginary part of Z_t. The latter method was chosen in this work, since the Cole–Cole extrapolation can introduce

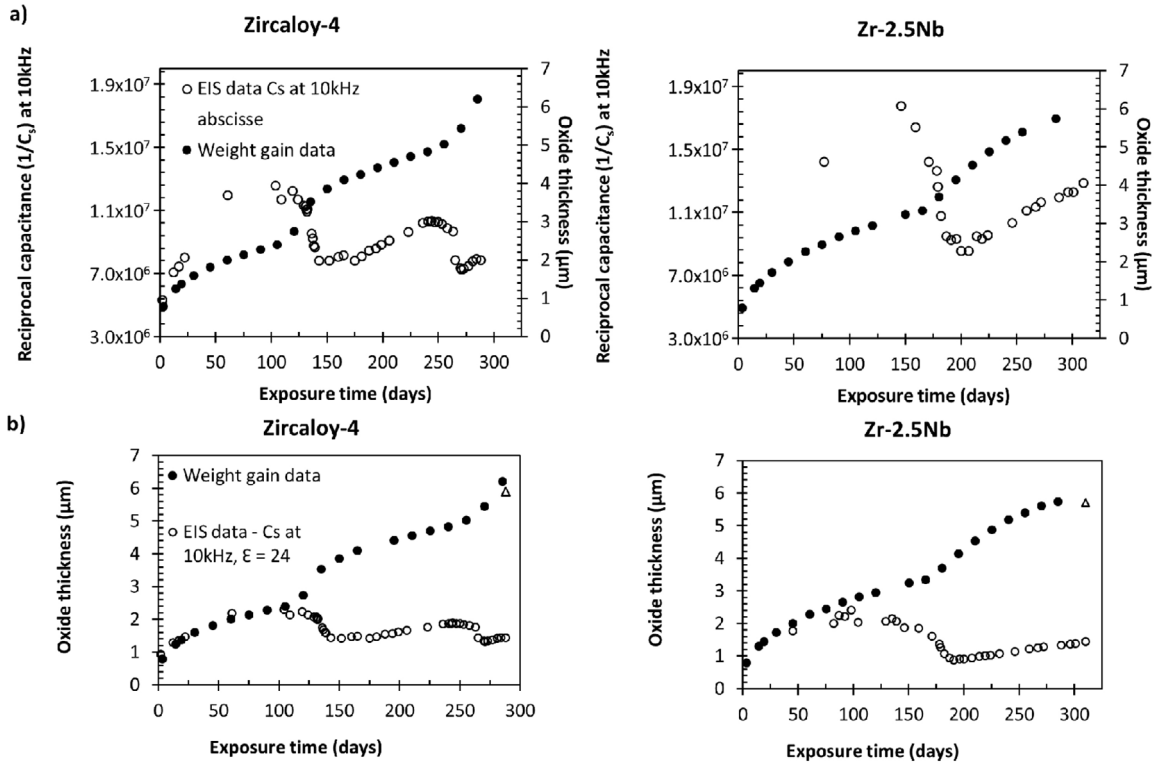

Fig. 8. (a) Reciprocal series capacitance $1/C_s$ determined at 10 kHz for Zircaloy-4 and Zr-2.5Nb alloys as function of exposure time. (b) Resulting oxide thickness using (7) and $\varepsilon_{ox} = 24$. The weight gain data are plotted as well as the SEM results as discussed in the discussion part.

errors in the evaluation of the oxide capacitance especially at the oxide transition [13].

The reciprocal series capacitance evaluated at 10 kHz is plotted as function of exposure time for Zircaloy-4 and Zr-2.5Nb alloys in Fig. 8 (a) along with the experimental weight gain data.

Examining Fig. 8(a), it can be noted that the reciprocal capacitance variations follow the same periodicity as the oxidation kinetics and are thus related to the oxide thickness. Oxide thickness can be derived from (5) and is plotted for both alloys in Fig. 8(b). For the oxide thickness measured by EIS to fit the weight gain measurements at early exposure times, a constant oxide relative permittivity ε_{ox} equal to 24 has been chosen. This value is in very good agreement with other values reported in the literature (i.e. between 13 and 30) [35–39]. One can notice a significant difference between weight gain and EIS data after the 1st oxide transition. Indeed, at oxide transitions, the oxide thickness measure by EIS drops to close to its original value whereas the weight gain keeps increasing. This is expected, since the weight gain measures the *total* oxide mass whereas EIS measures the *protective* oxide thickness. At oxide transitions, the oxide loses its protectiveness, and thus the protective oxide thickness disappears. Consequently, the reciprocal capacitance drops to its original value. After oxide transitions, the reciprocal capacitance starts increasing again, following the growth of a new protective oxide layer at the oxide/metal interface. In conclusion, the thickness of the oxide protective layer can be directly evaluated from in-situ from EIS measurements. This is another strong evidence that actual oxide properties can be quantitatively measured by in-situ EIS.

4.3.3. Oxide thickness measurements after EIS experiment

The EIS results obtained in this study have shown that impedance measurement is a suitable technique to measure oxide thickness in-situ. SEM characterization of the oxide layer has also been performed at the end of corrosion tests on both alloys to verify if the oxidation kinetics of the sample at the end of the EIS tests is similar to the sister sample oxidation kinetics performed in previous experiments. Scanning Electron Microscope (SEM) micrographs, performed on a LEO 1530 at the Materials Science Center at the University of Wisconsin-Madison, are presented in Fig. 9 showing the oxide layer formed in Zircaloy-4 and in Zr-2.5Nb samples. Similar oxide measurements made using SEM and averaged over multiple locations in the oxide have been performed. According to multiple measurements across the sample, the average oxide thickness formed on the Zircaloy-4 sample is equal to 5.9 µm and to 5.7 µm for the Zr-2.5Nb sample.

The oxide thicknesses determined by SEM have been added to Fig. 8 as triangles. Also, two layers of horizontal cracks in the oxide are clearly observed in Fig. 9 (left) for Zircaloy-4 whereas only one layer of cracks is seen in the oxide bulk in Fig. 9 (right) for Zr-2.5Nb, which have been commonly associated with the oxide transition (another layer of cracks is observed really close to the oxide/metal interface suggesting that this sample was archived right at the second transition as suggested in Fig. 8(b)). These cracks have been observed multiple times in the field of zirconium alloy corrosion and indicate the occurrence of the oxide transitions [40]. The corrosion of zirconium alloys proceeds through the formation of an oxide layer that is nearly equal to 1.57 times thicker than the metal it consumes. As a result, if this process occurs perfectly, meaning that all the volume expansion due to oxide formation occurs in the growth direction of the oxide, no strains are expected to accumulate in the growing oxide. However, even small departures from this ideal *behavior* lead to stress accumulation in the oxide layer, eventually causing horizontal cracks to form. These cracks then can help to create a percolation condition such that the water can easily access the oxide-water interface leading to the oxide kinetic transition and a sudden increase in corrosion rate [4]. This easy access of water to the metal increases the corrosion rate, as observed in weight gain, EIS and SEM measurements. Indeed, the distances

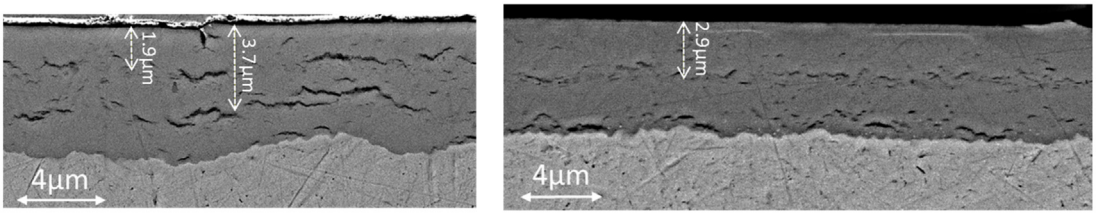

Fig. 9. SEM (secondary electrons) micrographs of oxide layers on left Zircaloy-4 and on right Zr-2.5Nb at the end of corrosion tests.

between these cracks and from first cracks to the oxide/metal interface measured by metallography are in very good agreement with the sudden increase in corrosion rate observed in weight gain and in the decrease of capacitance observed in EIS measurements, as also observed previously [15]. These agreements are an additional evidence that oxidation kinetics can be precisely monitored using in-situ EIS.

In conclusion, in-situ EIS is a suitable non-destructive technique to precisely measure zirconium alloys oxidation kinetics in-situ. This is proved by multiple evidences: (i) evolution of the impedance spectra as function of exposure time, (ii) correlations between oxidation kinetics determined from EIS spectra and oxidation kinetics determined from weight gain measurements and metallography. However, it is still uncertain that the oxide resistivity can be measured as function of exposure time using in-situ EIS. Indeed although these results tend to show that the variations in are related to the oxide real impedance R_{ox} such that the oxide resistivity ρ_{ox}^{EIS} could be confidently measured from EIS processed spectra, one cannot rule out that, from (7), the oxide/water interface impedance $R_{ox/e}$ contributes to Re $\left(\lim_{\omega\to 0} Z_t\right)$. Evidences that $R_{ox/e}$ is negligible are provided in the next section.

4.3.4. Zirconium alloys impedance spectra as function of lithium content

In order to evaluate the influence of the oxide/water interfacial impedance on the real impedance recorded at low frequency Re $\left(\lim_{\omega\to 0} Z_t\right)$, EIS spectra of a pre-corroded Zircaloy-4 sample ($\delta\sim 1\,\mu m$) were acquired in electrolytes with different Li concentrations (2.2 ppm, 4.4 ppm and 8.8 ppm). It has indeed been shown that Li should at least have an impact on the oxide/water interfacial reaction [41]. It has also been shown that at these low concentrations, although Li has an effect on the interface, it does not affect the oxidation kinetics [42]. If no measurable influence of Li concentrations is observed on the low frequency impedance of the EIS processed spectra then one can be confident that Re $\left(\lim_{\omega\to 0} Z_t\right) \sim R_{ox}$. The averaged real impedance (between 10^{-4} and 10^{-3}Hz) of the electrochemical cell is plotted as function of the electrolyte Li concentrations in Fig. 10 after the electrolyte resistance has been subtracted from the EIS data. Clearly, no significant influence of Li concentrations on the low frequency system impedance is observed, up to a concentration of 8.8 wt ppm of Li. This provides another strong argument that Re $\left(\lim_{\omega\to 0} Z_t\right) \sim R_{ox}$. Thus, oxide resistivity ρ_{ox}^{EIS} can be quantitatively measured as shown in Table 3.

Table 3
Approximated total system impedance and related oxide properties as function of the EIS frequency domain.

Frequency domain	$\omega \to 0$	$\omega \gg 1$	$\omega \to \infty$
Approximated impedance after processing	R_{ox}	$-\frac{j}{\omega C_{ox}}$	0
Determined oxide properties	ρ_{ox}^{EIS}	δ_{ox}	

4.4. Oxide resistivity

4.4.1. Oxide resistivity measurements

The oxide resistivity (ρ_{ox}^{EIS} in Ω cm) is calculated from low-frequency impedance Re $\left(\lim_{\omega\to 0} Z_t\right)$ measurements multiplied by a geometrical factor:

$$\rho_{ox}^{EIS} = S\frac{\mathrm{Re}\left(\lim_{\omega\to 0} Z_t\right)}{\delta_{ox}} \quad (8)$$

with δ_{ox} the protective oxide thickness determined by EIS in cm (see Fig. 8), S the sample surface in cm^2 and Re $\left(\lim_{\omega\to 0} Z_t\right)$ the real impedance in Ω averaged over one decade from 300 µHz to 3mHz. An average value has been chosen as an approximation of $\lim_{\omega\to 0} Z_t$ rather than an interpolation at $\omega \to 0$ from Nyquist diagram because of significant uncertainty inherent in such an interpolation. Because of this, the measured oxide resistivity represent a value that is lower than the exact oxide resistivity. It is emphasized that oxide *resistivity*, as calculated using (8), is independent of oxide thickness whereas oxide *resistance* R_{ox} increases as the oxide grows. The oxide resistivity (in $10^6\,\Omega$ cm) as function of exposure time for the two alloys is plotted in Fig. 11 along with the oxide thickness from weight gain.

The oxide resistivity ρ_{ox}^{EIS} should be independent of oxide thickness. However, it is observed in Fig. 11 that the oxide resistivity as measured by EIS varies as function of exposure time, indicating a change in oxide properties related to the transport of charged species through the oxide as the oxide grows.

For both alloys studied, the oxide resistivity varies with the same periodicity as the oxidation kinetics and is thus clearly related to oxide transitions. In the pre-transition regime (before the 1st transition), ρ_{ox}^{EIS} increases for both alloys. At transition, the resistivity suddenly drops, but increases quite rapidly right after the transition to reach a plateau for the Zircaloy-4 alloy, whereas it steadily decreases for the Zr-2.5Nb alloy. For Zircaloy-4, these variations are repeated in the similar form at the second transition.

It is also observed that quantitatively ρ_{ox}^{EIS}(Zr4) varies from 0.3GΩ cm to 1GΩ cm whereas ρ_{ox}^{EIS}(Zr − 2.5Nb) varies from

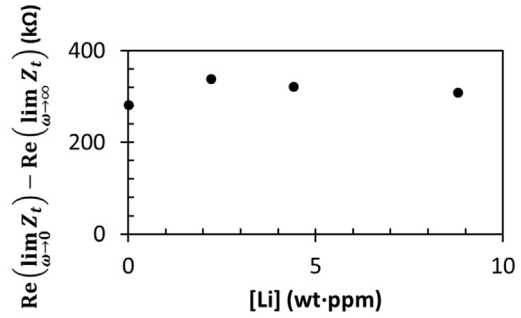

Fig. 10. Averaged low frequency impedance as function of electrolyte Li concentration for the Zr/Pt electrochemical cell.

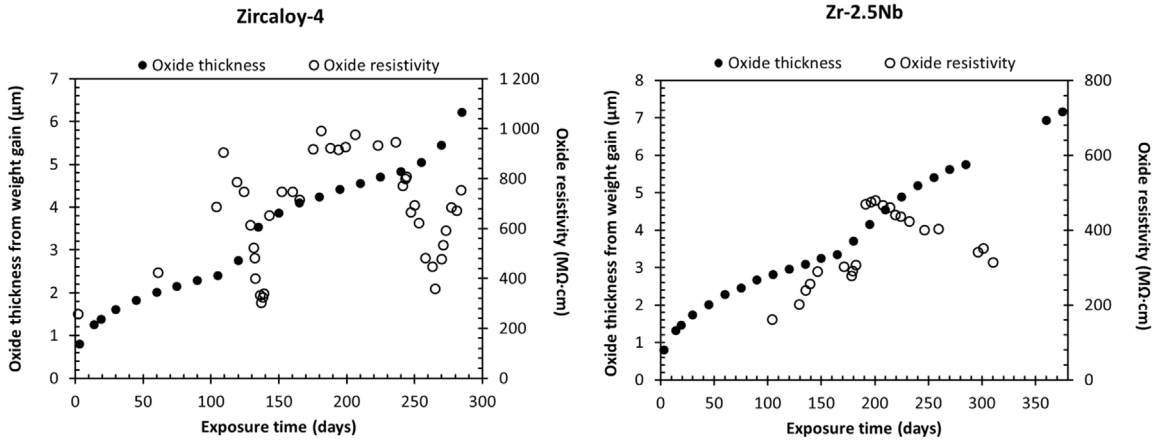

Fig. 11. Oxide resistivity for Zircaloy-4 and Zr-2.5Nb alloys as function of exposure time. The oxide thickness data (from weight gain) are also plotted.

0.2 GΩ cm to 0.5 GΩ cm. Thus the resistivity of Zircaloy-4 as measured by EIS is approximately twice as high as the resistivity of Zr-2.5Nb, indicating a higher resistance to charged species transport through the oxide grown on Zircaloy-4 as compared to Zr-2.5Nb. As noted before, there is also a difference between the two alloys in the period between the 1st and 2nd transitions. During this period, ρ_{ox}^{EIS} (Zr4) remains constant whereas ρ_{ox}^{EIS} (Zr − 2.5Nb) slightly decreases. The following part is dedicated to the correlation between oxide resistivity and hydrogen pickup.

5. Discussion and relation to hydrogen pickup

As discussed before, the corrosion mechanism developed in [1,17] suggests that there is a relationship between ρ_{ox}, the oxide resistivity, and f_H, the hydrogen pickup fraction, which predicts that f_H increases with ρ_{ox}. One of the goods of this paper was to verify this prediction by directly measuring the oxide resistivity in these two alloys and plot it as function of hydrogen pick-up.

In Fig. 12, the oxide resistivity of the two alloys (Zircaloy-4 and Zr-2.5Nb) at different stages of corrosion is plotted as function of *instantaneous*[2] hydrogen pickup fraction (f_H^i). The f_H^i is defined as the ratio of the hydrogen absorbed between time t and time $t + \Delta t$ to the total amount of hydrogen generated by the corrosion reaction during the same time increment [2,19]. Two things are observed in Fig. 12, (i) the resistivity of the oxide layer formed on Zircaloy-4 is greater than the resistivity of the oxide layer formed on Zr-2.5Nb and (ii) for both alloys, the instantaneous hydrogen pickup fraction is proportional to the oxide resistivity (i.e. when the oxide resistivity increases, f_H^i increases proportionally). That is, as the oxide resistivity increases, electron transport through the oxide layer becomes more difficult, which leads to ingress of hydrogen, and to higher hydrogen pickup.

The following explanation is thus proposed. Firstly, it is clearly observed in Fig. 12 that the resistivity of the oxide layer formed on the Zircaloy-4 alloy ρ_{ox}^{EIS} (Zr4) is two to three times higher than the resistivity of the oxide layer formed on Zr-2.5Nb ρ_{ox}^{EIS} (Zr − 2.5Nb). The lower Zr-2.5Nb alloy oxide resistivity compared to Zircaloy-4 oxide resistivity in similar environment has also been observed by others [43]. This effect is likely due to the doping of Nb aliovalent ions embedded in the oxide, which would decrease the amount of positive space charge in the oxide and thus lower the electronic oxide resistivity [1,17,22,27,29].

Consequently, the electric field across the oxide (the driving force for proton absorption in the oxide as detailed in the general hypothesis §2) is lower in Zr-2.5Nb alloys and thus fewer protons are absorbed leading to a lower hydrogen pickup fraction. In the case of Zircaloy-4, there are not enough Fe or Cr aliovalent ions embedded in solid solution in the oxide to compensate the space charges because of their extremely low solubility limit in metal (at least an order of magnitude lower than the Nb solubility limit). The electric field would be higher than in the oxide of Zr2.5Nb.

Thus the in-situ EIS oxide resistivity measurements are coherent with the mechanism proposed above and show that oxide resistivity is an important factor in hydrogen pickup mechanism. These results clearly show that one possibility to design better alloys with limited hydrogen uptake is to optimize the alloying element content such as to reduce the electronic oxide resistivity.

Fig. 12 also shows that, for a given alloy, the electronic oxide resistivity increases as the protective oxide grows, in the period before the 1st transition or in the period between the 1st and 2nd transitions. This observation suggests that the increase in oxide resistivity is either due to a degradation of the oxide layer in terms of electron transport or to a build-up of space charges as the oxide grows. A degradation of the oxide layer is likely due to a change in precipitate state (metallic to oxidized) [22,44,45], in aliovalent ion concentrations [22] or in compressive stress in the oxide [46]. All these could potentially alter electron transport via changes in defect energy levels in the band gap. It also been clearly shown by the Coupled Current Charge Compensation (C4) model that oxide space charges build up as the oxide grows [17,27]. The increase in oxide resistivity during a period between two transitions results in an increase in the driving force for proton absorption (and in f_H^i as observed in [2]).

It is also interesting to notice that for a given oxide resistivity in Zircaloy-4, f_H^i is higher from a transition regime to the next as shown by the linear fits at the different transition regimes. For instance when ρ_{ox}^{EIS} (Zr4) is approximately equal to 0.8 GΩ cm, f_H^i is approximately equal to 20% in the pre-transition regime, 35% in the 1st transition regime and 45% in the 2nd transition regime. This increase in f_H^i from one transition to the next has been noticed previously but the current data confirms that this increase does not occur because of a resistivity increase. Thus, this particular increase in f_H^i from a transition regime to the next is not due to an alteration of electron transport in the protective oxide layer. An increase in hydrogen pressure at the oxide/water interface could potentially cause the observed increase in f_H^i from one transition to the next. Previous studies have indicated that hydrogen overpressure can increase hydrogen pick-up in zirconium alloys [47].

[2] The term instantaneous is defined on a time increment (or an oxide thickness increment) and is not really instantaneous but depends on the defined increment [2].

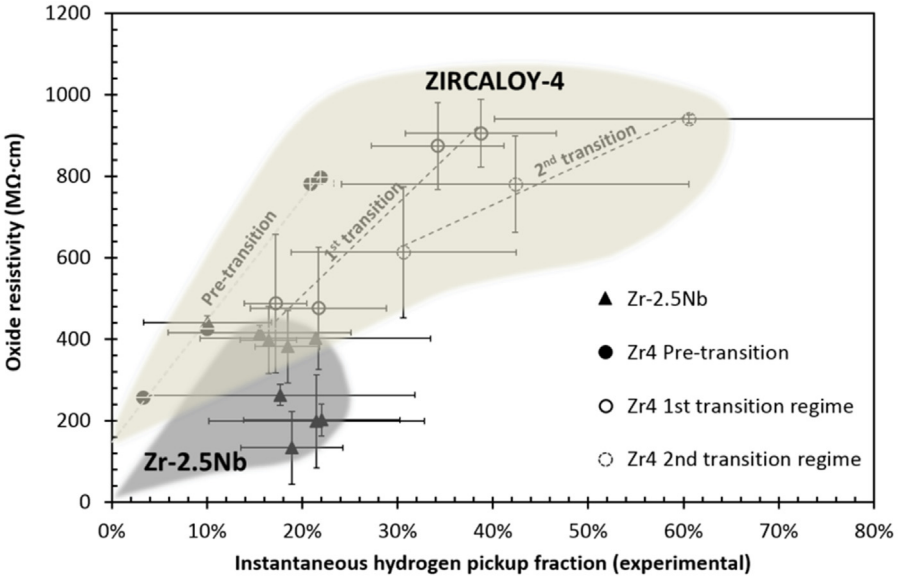

Fig. 12. Zircaloy-4 and Zr-2.5Nb oxide resistivity in MΩ cm as function of instantaneous hydrogen pickup fraction measured experimentally.

In the pre-transition regime the cathodic site is directly in contact with water, so that the hydrogen pressure at the cathodic site and in the water are equal. However, when a non-protective oxide layer is present on the top of the growing protective oxide (see Fig. 9), the hydrogen evolved at the cathodic site has to diffuse through these layers to finally reach the water. As a result, a hydrogen pressure gradient will be established across the non-protective oxide layers. This would cause hydrogen overpressure at the hydrogen evolution site to build up and could lead to an increase in f_H^i.

Thus, for a given alloy, the increase in f_H^i during a period between two transitions is due to an increase in oxide resistivity caused by an alteration of electron transport through the *protective* oxide. However, the increase in f_H^i between two transitions is likely due to an increase in hydrogen pressure at the oxide/water interface because of the presence of *non-protective* oxide layers.

6. Conclusions

In-situ Electrochemical Impedance Spectroscopy experiments have been performed on Zircaloy-4 and Zr-2.5Nb alloys during corrosion in water at 360 °C. The oxide thickness and oxide resistivity of these two alloys were measured as function of exposure time. After the different hypotheses were verified, the main conclusions obtained are summarized below

1. In zirconium alloys, the oxide resistivity has a proportional relationship with *instantaneous* hydrogen pickup fraction. This observation supports the hypothesis that oxide electronic resistivity is a key parameter in hydrogen absorption of zirconium alloys. As the oxide grows, the oxide transport properties are altered, which results in an increase of oxide resistivity. Consequently, the electric potential across the oxide increases which acts to speed up the electron transport. However, this increase in oxide electric potential also results in a stronger driving force for proton absorption by the metal. When hydrogen is absorbed, the cathodic reaction occurs in the oxide (or even at the oxide/metal interface) resulting in hydrogen *pickup* rather than in hydrogen evolution. The increase in driving force (i.e. oxide electric potential) is thus directly balanced by an increase of its effect (i.e. hydrogen pickup).
2. The EIS results show that the resistivity of the oxide layer formed on Zircaloy-4 is higher that the resistivity of the oxide layer formed on Zr-2.5Nb. Thus, as observed previously, the hydrogen pickup fraction of Zircaloy-4 is higher than the hydrogen pickup fraction of Zr-2.5Nb alloy according to the formulated hydrogen pickup mechanism. That is, as the oxide resistivity increases, electron transport through the oxide layer becomes more difficult, which leads to ingress of hydrogen to “close” the cathodic reaction, and to higher hydrogen pickup.
3. The oxide thickness evolution followed in-situ using a high-frequency capacitance as the oxide dielectric capacitance showed that, in the pre-transition regime, the EIS measurements of oxide thickness match the weight gain and electron microscope measurements of the oxide thickness. After the first transition, the oxide thickness measured by EIS corresponds to the newly formed protective oxide thickness rather than to the entire oxide.
4. EIS impedance spectra show a decrease in the oxide impedance just before the oxide transition (as deduced from weight gain). Thus, the oxide transition is not an instantaneous process but is better described by a gradual loss of oxide layer protectiveness.
5. The oxide *resistivity* evolution is measured using the low-frequency real impedance. The oxide resistivity varies with exposure time (increases up to the transition and decreases at transition) indicating a degradation of the charged species transport properties of the oxide layer. The nature of this degradation is not known at the moment but could be related to the delayed oxidation of alloying elements incorporated into the oxide layer, either in solid solution or as precipitates or to the build-up of space charges in the bulk oxide.

Acknowledgments

Funding for part of this research was provided by the MUZIC-2 (Mechanistic Understanding of Zirconium Corrosion). We are grateful for the support as well as for helpful discussions with Thierry Ghys and Martin Bachet of EDF R&D division and with the community of the MUZIC-2 research program.

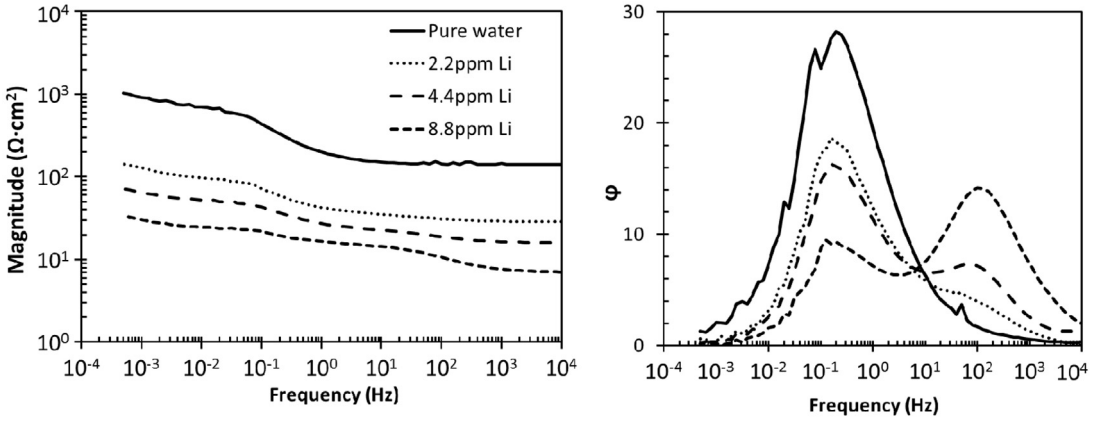

Fig. A1. Bode plots (modulus and phase) of the Pt/Pt electrochemical cell for different Li concentrations.

Appendix A.

The dummy cell was used to measure the electrolyte conductivity at 360 °C and 18 MPa as function of Li concentrations to validate that $\lim_{\omega\to\infty} Z_t \sim R_e$. The starting electrolyte was pure water into which LiOH injections were performed to reach Li concentrations of 2.2 ppm, 4.4 ppm and 8.8 ppm. Li concentrations were measured from electrolyte samples before any further injection in the autoclave by Inductively Coupled Plasma Mass Spectrometry.

The Bode plots of the dummy cell impedance spectra acquired at different LiOH concentrations are presented in Fig. A1. As expected, the modulus of the impedance decreases as the LiOH concentration in the electrolyte increases. The impedance of the electrolyte is measured at high frequency (between 103 Hz and 104 Hz) and is reported in Fig. A2 along with the theoretical electrolyte conductivity as calculated in the following. The calculated theoretical impedance matches the measured impedance, such that these results tend to validate the experimental setup.

The geometry of the Pt tube/Pt ref electrode cell is similar to a cylindrical capacitor of length L as seen in Fig. A3.

$r_1 < r < r_2$ the total current I is defined in terms of current density j as:

$$I = \iint \vec{j}\cdot d\vec{S} = \iint \vec{j}\cdot dS.\vec{e_r} = \iint j_r \cdot dS = 2\pi r L j_r \tag{A.1}$$

Locally, Ohm's law is defined as:

$$\vec{j} = \sigma\vec{E} \rightarrow j_r = \sigma E_r = -\sigma\frac{\partial V}{\partial r} \tag{A.2}$$

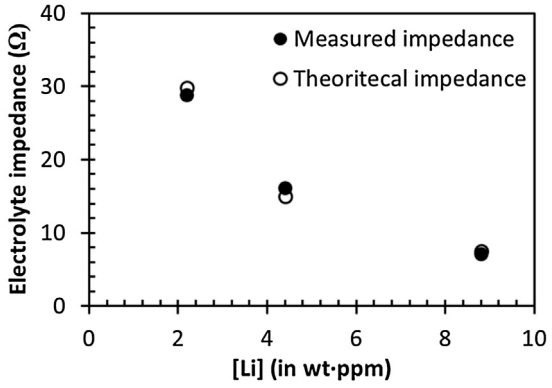

Fig. A2. Bode plots (modulus and phase) of the Pt/Pt electrochemical cell for different Li concentrations.

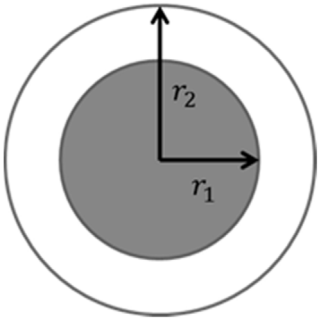

Fig. A3. Top view schematic of the cell geometry.

Thus:

$$\int dV = -\int \frac{j_r}{\sigma} dr = -\frac{I}{2\pi\sigma L}\int \frac{dr}{r} = \frac{I}{2\pi\sigma L}\ln\left(\frac{r_1}{r_2}\right) \tag{A.3}$$

Thus the electrolyte impedance is equal to:

$$R_e = \frac{1}{2\pi\sigma L}\ln\left(\frac{r_1}{r_2}\right)$$

The limiting ionic conductance λ of Li^+ and OH^- (in $S\,cm^2$) have been found in the literature at different temperatures up to 300 °C [48]. An interpolation has been done to estimate the limiting ionic conductance at 360 °C. The specific ionic conductivity of the electrolyte can be determined using the following formula:

$$\sigma = \frac{d_w}{1000}10^{-3}\Sigma m_i\lambda_i \tag{A.4}$$

where m_i is in wt ppm and d_w is the density of water at temperature. The density of water at 360 °C and 180 bar is equal to 0.53 g/cm^3 [49]. Thus, the theoretical impedance of the electrolyte can be calculated and is displayed in Fig. A2 for various concentrations of LiOH with $r_1 = 0.5$ cm and $r_2 = 0.75$ cm.

References

[1] A.T. Motta, A. Couet, R.J. Comstock, Corrosion of zirconium alloys used for nuclear fuel cladding, Annu. Rev. Mater. Res. 45 (18) (2015) 11–33.
[2] A. Couet, A.T. Motta, R.J. Comstock, Hydrogen pickup measurements in zirconium alloys: relation to oxidation kinetics, J. Nucl. Mater. 451 (2014) 1–13.
[3] H.A. Porte, J.G. Schnizlein, R.C. Vogel, D.F. Fischer, Oxidation of zirconium and zirconium alloys, J. Electrochem. Soc. 107 (1960) 506–515.
[4] A.T. Motta, M.J. Gomes da Silva, A. Yilmazbayhan, R.J. Comstock, Z. Cai, B. Lai, Microstructural characterization of oxides formed on model Zr alloys using

synchrotron radiation, in: Zirconium in the Nuclear Industry: 15th International Symposium, ASTM STP 1505, 2009, p. 486.
[5] M. Tupin, M. Pijolat, F. Valdivieso, M. Soustelle, A. Frichet, P. Barberis, Differences in reactivity of oxide growth during the oxidation of Zircaloy-4 in water vapour before and after the kinetic transition, J. Nucl. Mater. 317 (2003) 130–144.
[6] S. Kass, The development of the zircaloys, USAEC Symposium on Zirconium Alloy Development, GEAP-4089, Castlewood, Pleasanton, CA, 1962.
[7] A.A. Kiselev, Research on the Corrosion of Zirconium Alloys in Water and Steam at High Temperature and Pressure, Atomic Energy of Canada Limited, 1963.
[8] H. Gohr, J. Schaller, H. Ruhmann, F. Garzarolli, Long-term in situ corrosion investigation of Zr alloys in simulated PWR environment by electrochemical measurements, in: Zirconium in the Nuclear Industry: Eleventh International Symposium, ASTM STP 1295, 1996, pp. 181–202.
[9] M. Tupin, C. Bataillon, J.-P. Gozlan, P. Bossis, High temperature corrosion of Zircaloy-4, in: R.W. Bosch, D. Féron, J.P. Celis (Eds.), Electrochemistry in Light Water Reactors: Reference Electrodes, Measurement, Corrosion and Tribocorrosion Issues, European Federation of Corrosion, 2007, pp. 134–163.
[10] J. Schefold, D. Lincot, A. Ambard, O. Kerrec, The cyclic nature of corrosion of Zr and Zr-Sn in high-temperature water (633 K)—a long-term in situ impedance spectroscopic study, J. Electrochem. Soc. 150 (2003) B451–B461.
[11] S. Forsberg, E. Ahlberg, M. Limback, Studies of corrosion of cladding materials in simulated BWR environment using impedance measurements, in: Zirconium in the Nuclear Industry: 15th International Symposium, ASTM STP 1505, West Conshohocken, 2009, pp. 303–325.
[12] M. Bojinov, V. Karastoyanov, P. Kinnunen, T. Saario, Influence of water chemistry on the corrosion mechanism of a zirconium-niobium alloy in simulated light water reactor coolant conditions, Corros. Sci. 52 (2010) 54–67.
[13] P. Barberis, A. Frichet, Characterization of zircaloy-4 oxide layers by impedance spectroscopy, J. Nucl. Mater. 273 (1999) 182–191.
[14] M.E. Orazem, I. Frateur, B. Tribollet, V. Vivier, S. Marcelin, N. Pebere, A.L. Bunge, E.A. White, D.P. Riemer, M. Musiani, Dielectric properties of materials showing constant-phase-element (CPE) impedance response, J. Electrochem. Soc. 160 (2013) C215–C225.
[15] A. Yilmazbayhan, A.T. Motta, R.J. Comstock, G.P. Sabol, B. Lai, Z. Cai, Structure of zirconium alloy oxides formed in pure water studied with synchrotron radiation and optical microscopy: relation to corrosion rate, J. Nucl. Mater. 324 (2004) 6–22.
[16] N. Ni, D. Hudson, J. Wei, P. Wang, S. Lozano-Perez, G.D.W. Smith, J.M. Sykes, S.S. Yardley, K.L. Moore, S. Lyon, R. Cottis, M. Preuss, C.R.M. Grovenor, How the crystallography and nanoscale chemistry of the metal/oxide interface develops during the aqueous oxidation of zirconium cladding alloys, Acta Mater. 60 (2012) 7132–7149.
[17] A. Couet, A.T. Motta, A. Ambard, The coupled current charge compensation model for zirconium alloy fuel cladding oxidation: I. Parabolic oxidation of zirconium alloys, Corros. Sci. 100 (2015) 73–84.
[18] D. Lazar, V. Ussui, Evaluation of the effect of heavy rare earth elements on electrical resistivity of zirconia-yttria ceramics, Mater. Sci. Forum 498–499 (2005) 305–310.
[19] A. Couet, A.T. Motta, R.J. Comstock, R.L. Paul, Cold neutron prompt gamma activation analysis, a non-destructive technique for hydrogen level assessment in zirconium alloys, J. Nucl. Mater. 425 (2012) 211–217.
[20] P. Moulart, Concentration en hydrogene dissous dans les milieux d'essais a haute temperature, in: Resultats Experimentaux, EDF R&D, 2002.
[21] A. Couet, A.T. Motta, R.J. Comstock, Effect of alloying elements on hydrogen pick-up in zirconium alloys, in: B. Comstock (Ed.), 17th International Symposium on Zirconium in the Nuclear Industry, ASTM STP1543, Hyderabad, 2013, pp. 479–514.
[22] A. Couet, A.T. Motta, B. de Gabory, Z. Cai, Microbeam X-ray absorption near-edge spectroscopy study of the oxidation of Fe and Nb in zirconium alloy oxide layers, J. Nucl. Mater. 452 (2014) 614–627.
[23] P.J. Shirvington, Electron conduction through oxide films on zircaloy-2, J. Nucl. Mater. 37 (1970) 177–202.
[24] M. Inagaki, M. Kanno, H. Maki, Effect of Alloying Elements in Zircaloy on Photoelectrochemical Characteristics of Zirconium-Oxide Films, ASTM STP 1132, Philadelphia, 1991.
[25] M.M.R. Howlader, K. Shiiyama, C. Kinoshita, M. Kutsuwada, M. Inagaki, The electrical conductivity of zircaloy oxide films, J. Nucl. Mater. 253 (1998) 149–155.
[26] H. Frank, Transport properties of zirconium alloy oxide films, J. Nucl. Mater. 306 (2002) 85–98.
[27] A. Couet, A.T. Motta, A. Ambard, R.J. Comstock, Hydrogen pickup mechanism in zirconium alloys, in: 18th International Symposium on Zirconium in the Nuclear Industry, Hilton Head Island, SC, 2016.
[28] H.-J. Beie, A. Mitwalsky, F. Garzarolli, H. Ruhmann, H.J. Sell, Examinations of the corrosion mechanism of zirconium alloys, in: Zirconium in the Nuclear Industry: Tenth International Symposium, ASTM STP1245, Philadelphia, PA, 1994, pp. 615–643.
[29] G.A. Eloff, C.J. Greyling, P.E. Viljoen, The role of space charge in the oxidation of Zircaloy-4 between 350 and 450 °C in air, J. Nucl. Mater. 199 (1993) 285–288.
[30] A. Couet, A.T. Motta, A. Ambard, R.J. Comstock, Oxide electronic conductivity and hydrogen pickup fraction in Zr alloys, in: 2014 Annual Meeting on Transactions of the American Nuclear Society and Embedded Topical Meeting: Nuclear Fuels and Structural Materials for the Next Generation Nuclear Reactors, NSFM 2014, ANS Transactions, Reno, NV, United States, 2014, pp. 845–848.
[31] C. Gabrielli, Identification of Electrochemical Processes by Frequency Response Analysis, Solartron Schlumberger, 1984.
[32] J.O.M. Bockris, A.K.N. Reddy, M. Gamboa-Aldeco, M.E. Gamboa-Aldeco, Modern Electrochemistry, Springer, 2000.
[33] B. Cox, Rate controlling processes during the pre-transition oxidation of zirconium alloys, J. Nucl. Mater. 31 (1969) 48–66.
[34] J.R. Macdonald, W.B. Johnson, Fundamentals of impedance spectroscopy, in: Impedance Spectroscopy, John Wiley & Sons Inc., 2005, pp. 1–26.
[35] B. Cox, Y. Yamaguchi, The development of porosity in thick zirconia films, J. Nucl. Mater. 210 (1994) 303–317.
[36] C. Bataillon, S. Brunet, Electrochemical impedance spectroscopy on oxide films formed on zircaloy 4 in high temperature water, Electrochim. Acta 39 (1994) 455–465.
[37] L. Young, Anodic Oxide Films, Academic Press London, New York (N.Y.), 1961.
[38] J.J. Vermoyal, A. Hammou, L. Dessemond, A. Frichet, Electrical characterization of waterside corrosion films formed on ZrNb(1%)O(0.13%), Electrochim. Acta 47 (2002) 2679–2695.
[39] P.J. Harrop, J.N. Wanklyn, The dielectric constant of zirconia, Br. J. Appl. Phys. 18 (1967) 739.
[40] B. Griggs, H.P. Maffei, D.W. Shannon, Multiple rate transitions in the aqueous corrosion of zircaloy, J. Electrochem. Soc. 109 (1962) 665–668.
[41] M. Oskarsson, E. Ahlberg, K. Pettersson, Oxidation of Zircaloy-2 and Zircaloy-4 in water and lithiated water at 360 °C, J. Nucl. Mater. 295 (2001) 97–108.
[42] E. Hillner, J.N. Chirigos, L. Bettis, U.S. Atomic Energy. The effect of lithium hydroxide and related solutions on the corrosion rate of zircalloy in 680F water. Westinghouse Electric Corporation. United States. Dept. of Commerce. Office of Technical, Pittsburgh, Pa., Washington, D.C. 1962.
[43] K. Baur, F. Garzarolli, H. Ruhmann, H.-J. Sell, Electrochemical examinations in 350 °C water with respect to the mechanism of corrosion-hydrogen pickup, in: Zirconium in the Nuclear Industry: Twelfth International Symposium, ASTM STP 1354, 2000, pp. 836–852.
[44] D. Pêcheur, F. Lefebvre, A.T. Motta, C. Lemaignan, J.F. Wadier, Precipitate evolution in the zircaloy-4 oxide layer, J. Nucl. Mater. 189 (1992) 318–332.
[45] B. de Gabory, A.T. Motta, K. Wang, Transmission electron microscopy characterization of zircaloy-4 and ZIRLO™ oxide layers, J. Nucl. Mater. 456 (2015) 272–280.
[46] G. Zumpicchiat, S. Pascal, M. Tupin, C. Berdin-Méric, Finite element modelling of the oxidation kinetics of zircaloy-4 with a controlled metal-oxide interface and the influence of growth stress, Corros. Sci. 100 (2015) 209–221.
[47] E. Hillner, Hydrogen Absoprtion in Zircaloy During Aqueous Corrosion, effect of environment, AEC Research and Development, 1964.
[48] The ASME Handbook on Water Technology for Thermal Power Systems, American Society of Mechanical Engineers, 1992.
[49] Revised Supplementary Release on Saturation Properties of Ordinary Water Substance, The International Association for the Properties of Steam and Water, 1992.